Optoelectronic properties of confined water in angstrom-scale slits

S. Shekarforoush,[1] H. Jalali,[2] M. Yagmurcukardes,[3,4,5] M. V. Milošević,[3,4] and M. Neek-Amal[1,3,*]

[1]*Department of Physics, Shahid Rajaee Teacher Training University, 16875-163 Lavizan, Tehran, Iran*

[2]*Department of Physics, University of Zanjan, 45195-313 Zanjan, Iran*

[3]*Department of Physics, University of Antwerp, Groenenborgerlaan 171, B-2020 Antwerp, Belgium*

[4]*NANOlab Center of Excellence, Groenenborgerlaan 171, B-2020 Antwerp, Belgium*

[5]*Department of Photonics, Izmir Institute of Technology, 35430 Izmir, Turkey*

(Received 31 August 2020; revised 2 November 2020; accepted 10 November 2020; published 4 December 2020)

The optoelectronic properties of confined water form one of the most active research areas in the past few years. Here we present the multiscale methodology to discern the out-of-plane electronic and dipolar dielectric constants ($\varepsilon_\perp^{\rm el}$ and $\varepsilon_\perp^{\rm dip}$) of strongly confined water. We reveal that $\varepsilon_\perp^{\rm el}$ and $\varepsilon_\perp^{\rm dip}$ become comparable for water confined in angstrom-scale channels (with a height of less than 15 Å) within graphene (GE) and hexagonal boron nitride (hBN) bilayers. Channel height (h) associated with a minimum in both $\varepsilon_\perp^{\rm el}$ and $\varepsilon_\perp^{\rm dip}$ is linked to the formation of the ordered structure of ice for $h \approx$ (7–7.5) Å. The recently measured total dielectric constant $\varepsilon_\perp^{T}$ of nanoconfined water [L. Fumagalli *et al.*, Science **360**, 1339 (2018)] is corroborated by our results. Furthermore, we evaluate the contribution from the encapsulating membranes to the dielectric properties, as a function of the interlayer spacing, i.e., the height of the confining channel for water. Finally, we conduct analysis of the optical properties of both confined water and GE membranes, and show that the electron energy loss function of confined water strongly differs from that of bulk water.

DOI: 10.1103/PhysRevB.102.235406

I. INTRODUCTION

Optical, dielectric, and electronic properties of confined water in hydrophobic (e.g., made of GE) and hydrophilic (e.g., hBN) slit-shaped pores and channels are of broad relevance to science and engineering, in topics as versatile as ion-transfer and protein folding [1,2], biochemistry, environmental science [3], and fluid-based electronics [4,5]. One generally expects a very low dielectric constant in crystalline two-dimensional (2D) materials [6], but only recently it became possible to measure the out-of-plane dielectric constant of confined water by detection of electrostatic force via atomic-force microscopy (AFM) [7]. For water confined within bilayer GE and bilayer hBN it was found that the total out-of-plane dielectric constant of water is $\varepsilon_\perp^{T} \approx 2$ for channel height smaller than 15 Å [7] (while the dielectric constant of GE and hBN layers was measured to be about 3.5). Such ultralow $\varepsilon_\perp^{T}$ is below any reported dielectric constant of water and ice, and might be due to the formation of two interfacial layers close to the confining membranes having vanishingly small polarizations. For channel heights $h > 20$ Å, the dielectric constant increases superlinearly towards the bulk value ($\varepsilon_B \approx 80$) [7]. One then poses the question: What is the structure of such a strongly confined water? The formation of ice under such high-pressure conditions is expected. Independent of the water phase, all the ice phases formed under pressure should satisfy the so-called Bernal-Fowler ice rules, where each water molecule has four hydrogen-bonded neighbors with a quasitetrahedral configuration [with two short O-H distances (the donated protons) and two long ones (the accepted protons)]. At the transition into 2D phase of ice, the crystalline structure with a larger density may form, where the nearest-neighbor distances are more or less the same. Such a flat square ice was proposed in Ref. [8], exhibiting higher density (1.36 gcm^{-3}) as compared to bulk crystalline ices ($\sim$0.92 gcm^{-3} for ice IX and XI). However, we will show that crystalline 2D ices cannot be the answer to the above question posed. If so, then it becomes impossible to infer how the electronic and dipolar contributions to dielectric constant of water will evolve in the regime of the angstrom-scale confinement. The prediction of the latter behavior is the primary objective of our paper.

Although several studies determined the out-of-plane component of dipolar dielectric constant of confined water in nanoscale channels [9–12], there is no clear distinction nor explanation for the behavior of either electronic or dipolar dielectric constant of confined water in channels narrower than 15 Å. Since classical theoretical methods are unable to properly address the electronic part of the dielectric constant [8], quantum simulations at the angstrom length scale are highly required.

In this study, employing a multiscale approach, a solid theoretical background for understanding the dielectric properties of strongly confined water is presented. In particular, for water confined at angstrom scale (within the bilayers of 2D materials) we revealed that the electronic and dipolar contribution to the dielectric constant are almost equal. This is entirely at odds with expectations for bulk water, where electronic contribution is negligible, or the expectations for crystalline 2D materials, where dipolar contributions vanish. Besides the results on the confined water alone, we also present a separate yet useful analysis of the dielectric and

*Corresponding author: mehdi.neekamal@gmail.com

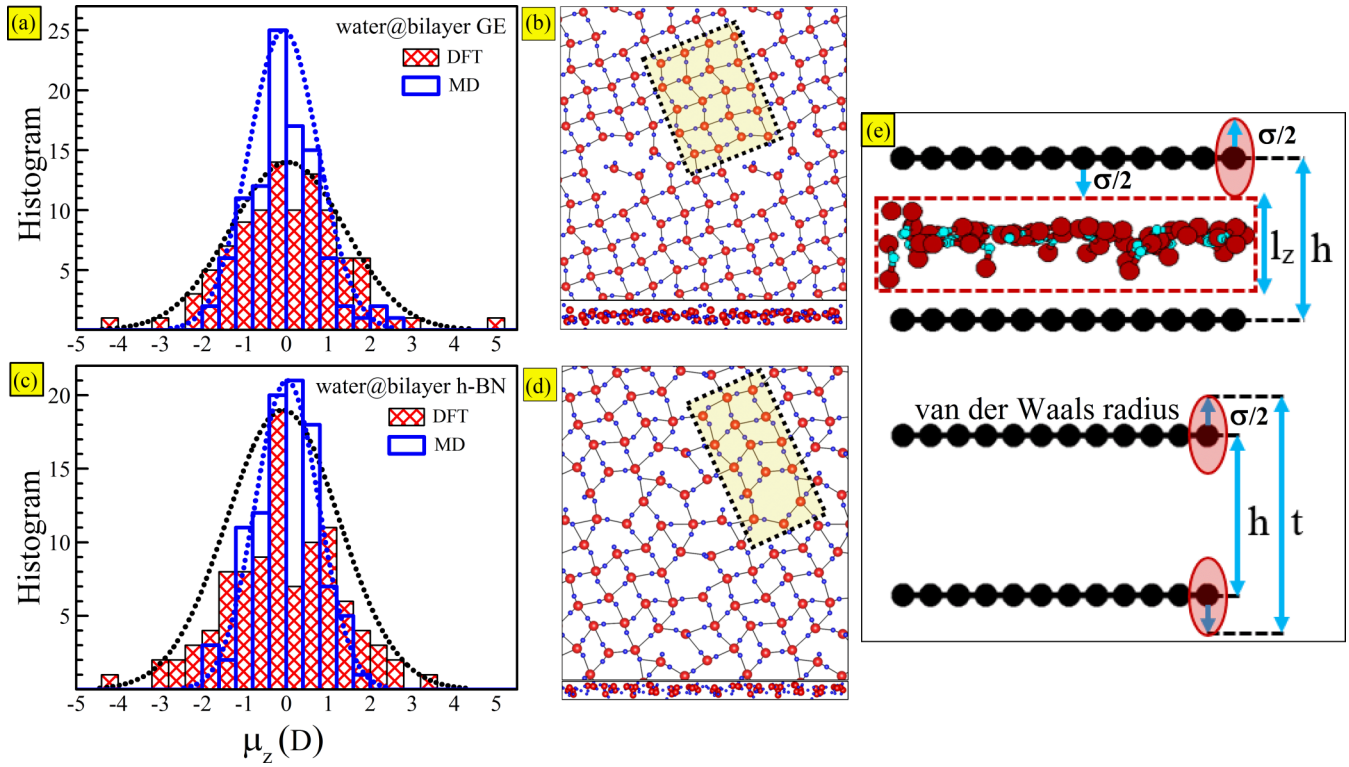

FIG. 1. The histogram for the z component of the dipolar and electronic dipole moments of (a) GE-confined water and (c) hBN-confined water, obtained from MD (empty columns) and DFT (shaded columns) calculations, in the absence of electric field. The blue and black dotted curves represent approximately Gaussian distribution. Panels (b) and (d) show the top and side views of the amorphous ice structures between GE and hBN layers under pressure (2–4) GPa and at room temperature, for channel height 7.2 Å. (e) illustrates the definition of different quantities: h, the distance between the centers of atoms of the confining layers; σ, the length parameter in the Lennard-Jones (LJ) potential; t, the effective (real) thickness of the system, with membranes included; l_z, the thickness of confined water alone.

optical properties of the confining GE or hBN membranes as a function of the interlayer distance, for complete understanding of related and readily feasible nanofluidic optoelectronic devices.

II. MULTISCALE APPROACH TO DIELECTRIC CONSTANT OF CONFINED WATER

We start by explaining the methodology behind our analysis. In order to extract the components to dielectric constant of confined water, we resort to the linear-response regime and employ two methods based on computing the z component of the total dipole moment. More details can be found in Ref. [13].

A. Dipolar contribution

Using the large scale atomic/molecular massively parallel simulator (LAMMPS) [14] package, after reaching equilibrium conditions during 9 ns, we produced hundreds of snapshot for confined water over the period of 1 ns. The cell length along the z axis was changed by sub-Angstrom steps of about 0.2 Å. Although in all plots channel height h was defined as the distance between the center of two C(B/N) atoms of top and bottom GE(hBN) layers, here we considered the effective height of water alone, i.e., $l_z = h - \sigma$ where σ is the length parameter in the Lennard-Jones (LJ) potential [cf. Fig. 1(c)].

The NVT ensemble (Nose-Hoover thermostat) was used to keep temperature constant at 300 K [15]. The SPC/E model for water-water interaction [16] and LJ potential were employed for GE-water and hBN-water interactions. The cut-off for LJ and Coulomb potential was taken to be 10 Å. The LJ parameters are set to $\epsilon_{OO} = 0.1553$ kcal/mol, $\sigma_{OO} = 3.166$ Å. By applying particle-particle particle-mesh (PPPM) method, the long-range Coulomb interaction has been computed, having an accuracy of 10^{-4}. The water bonds and angles were fixed using SHAKE algorithm [17]. The periodic boundary conditions are applied along the x and y directions. The unit cell sizes are set to yield the bulk water density, i.e., 1 gcm^{-3}.

A microscopic picture of dielectric properties of confined water can be assessed by calculating the fluctuations of the total dipole moment of the system ($\mu_T^{\rm dip}$) at finite temperature. After equilibration, by extracting the z component of the total molecular dipole moment, $\mu_z^{\rm dip}$, one obtains the perpendicular dipolar dielectric constant as [10]

$$\varepsilon_\perp^{\rm dip} = 1 + \frac{\sigma_\perp^2}{\varepsilon_0 k_B T V}, \tag{1}$$

where $\sigma_\perp^2 = \langle \mu_z^{\rm dip} \mu_z^{\rm dip} \rangle - \langle \mu_z^{\rm dip} \rangle \langle \mu_z^{\rm dip} \rangle$ and V is the volume of the system [$V = A \times l_z$ where A is the area of the confining

wall (membrane) and $l_z < h$ is the effective thickness of the confined water]. For $\mu_z^{\rm dip}(= P_z^{\rm dip} \times V)$ obtained in molecular dynamics simulations, the averaging is performed over time, typically for longer than 1 ns after $\varepsilon_\perp^{\rm dip}$ has converged. Note that Eq. (1) is applicable only to homogeneous systems [12] and can be reformatted to have the usual form of the fluctuation dissipation theorem [18].

B. Electronic contribution

Ab initio simulations of the behavior of the confined water under electric field were performed using the Spanish initiative for electronic simulations with thousands of atoms (SIESTA) [19] package based on the density functional theory (DFT). Double-ζ plus two polarization functions (DZDP) basis set for expansion of the electron wave function were used. For the exchange-correlation functional we used generalized gradient approximation (GGA) with Perdew-Burke-Ernzerhof (PBE) pseudopotential [20] and nonlocal van der Waals density functional (vdW-DF) with Dion-Rydberg-Schröder-Langreth-Lundqvist pseudopotential [21]. The linear combination of atomic orbitals (LCAO) with the cutoff energy of 400 Ry in $3 \times 3 \times 1$ Monkhorst-Pack grids were used for channel heights 6.5 Å $\leqslant h \leqslant$ 15 Å. Notice that for optical calculations, we increased the Monkhorst-Pack grids and optical mesh to $100 \times 100 \times 1$ and $500 \times 500 \times 1$, respectively.

The optimized ionic coordinates of water molecules from MD simulations were fed as input for DFT calculations. Next, the self-consistent cycle (SCF) convergence was performed where the vacuum size in the z direction for all systems was set to 20 Å.

By applying external electric field, perpendicular to the (x, y) plane, and finding the z component of the electronic dipole moment of the system, $\mu_z^{\rm el}$, one can estimate the electronic dielectric constant as

$$\varepsilon_\perp^{\rm el} \simeq 1 + \frac{\Delta\mu_z^{\rm el}}{\varepsilon_0 V E_z}, \tag{2}$$

where $\Delta\mu_z^{\rm el} = \mu_z^{\rm el}(E_z) - \mu_z(0)$ is the dipole moment variation for confined water subjected to an electric field E_z. Here $\mu_z^{\rm el}(0)$ is the electric dipole moment in the absence of electric field. A linear fit of the data of $\Delta\mu_z^{\rm el}$ versus E_z using Eq. (2) will yield $\varepsilon_{\rm el}^\perp$ for various considered configurations.

In order to understand this equation, for a given E_z, one can find $\varepsilon_\perp^{\rm el} = \frac{E_z}{E_z - E_\perp^p}$ when E_z is the external electric field, and E_p is the response (or polarization) electric field, i.e., $E_\perp^p = \frac{\Delta\mu_z^{\rm el}}{V}\varepsilon_0 = \Delta P_z^{\rm el}\varepsilon_0$, where $\Delta P_z^{\rm el}$ is the change in polarization that can be calculated from first principles. Obviously, for small $\frac{\Delta\mu_z^{\rm el}}{\varepsilon_0 V E_z}$ one obtains Eq. (2). Similar analysis was used for determining dielectric constant of bulk MgO by Umari *et al.*, where $\varepsilon_\perp$ was found to be around 5.14 [22].

C. Total dielectric constant

For polarizable systems, the total dielectric constant (or equivalently dielectric constant) has two main contributions, i.e., a molecular and electronic one:

$$\varepsilon_{ij}^T = \varepsilon_{ij}^m + \varepsilon_{ij}^{\rm el}, \tag{3}$$

where $i, j = x,\ y,\ z$, and ε_{ij}^m and $\varepsilon_{ij}^{\rm el}$ are molecular and electronic dielectric constant, respectively. Also, $\varepsilon_{ij}^m = \varepsilon_{ij}^{\rm dip} + \varepsilon_{ij}^{\rm ion}$ where $\varepsilon_{ij}^{\rm dip}$ and $\varepsilon_{ij}^{\rm ion}$ are dipolar and ionic terms. Note that the dipolar term is dominant compared to the ionic term. In the result, we assumed that $\varepsilon_{ij}^m = \varepsilon_{ij}^{\rm dip}$. Hereafter label zz is replaced by $\perp$. At zero temperature the dipolar term vanishes (because $\sigma_\perp^2 = 0$) and dielectric constant has only electronic contribution. By increasing temperature, and in the 3D phase, the dipolar term should be taken into account. Notice that the molecular term includes both ionic and dipolar terms, where the dipolar term is dominant, due to the rigidity of water bond lengths and angles. In this study we focus on the perpendicular component of $\varepsilon_\perp^T$ for both electronic and dipolar terms.

One also expects to see the contribution of confining membranes to the dielectric constant. Before presenting the dielectric behavior of confining membranes (in Sec. 3), we first determine the dielectric constant of confined water alone. The needed quantities to compute the dipolar and electronic dielectric constants as explained in the previous sections were calculated using combined molecular dynamics (MD) and *ab initio* simulations. In what follows, we present those results.

D. Results for dielectric constant of confined water alone

As explained above, different configurations (minimum 100 snapshots for a given channel height) of confined water between two GE(hBN) sheets separated by distance h were extracted from MD simulations. In Fig. 1, we show the histograms for the obtained z component of the dipolar and electronic dipole moments, $\mu_z^{\rm dip}$ and $\mu_z^{\rm el}$, for confined water in bilayer GE [Fig. 1(a)] and bilayer hBN [Fig. 1(b)] for $h =$ 7.2 Å and $E_z = 0$. As indicated in Fig. 1(c) and mentioned before, the channel height (h) is defined as the interlayer distance between the confining 2D membranes. However, the actual volume used in Eq. (1) and Eq. (2) is $V = A \times l_z$. For simplicity, the GE and hBN sheets were taken rigid in the MD simulations, and the considered channel height was kept below 15 Å. The insets in both figures show top and oblique views of a typical lattice structure of confined water. Interestingly, both dipolar and electronic parts of the dipole moments follow approximately Gaussian distribution in Figs. 1(a) and 1(b). It is worthwhile to estimate $\varepsilon_\perp^{\rm dip}$ using other water models such as TIP4P [23]. We performed an additional simulation to obtain $\varepsilon_\perp^{\rm dip}$ for nanoconfined water between two GE sheets with $h =$ 10 Å and found $\varepsilon_\perp^{\rm dip} \approx 3$ which is larger than the experimental value [7], i.e., 2. The latter results indicate that the SPC/E model produces better agreement with experimental results.

In the MD simulations, we computed the dipolar dielectric constant ($\varepsilon_\perp^{\rm dip}$) for various channel heights using Eq. (1). Then, for the electronic part, as depicted in Fig. 2 for two typical systems, we find the variation of electronic polarization ($P_z^{\rm el}$) with respect to the applied electric field, where the slope of $P_z^{\rm el}(E_z)$ for the considered confined water and Eq. (2) yield $\varepsilon_\perp^{\rm el}$.

The corresponding $\varepsilon_\perp^{\rm el}$ and $\varepsilon_\perp^{\rm dip}$ (without GE and hBN layers), using 100 MD snapshots and Eq. (2), are shown in Fig. 3 by square and triangular dots, respectively. In the same panel the total dielectric constant is shown by circular dots. Notice that we subtract 1 from $\varepsilon_\perp^T$ to avoid double counting, since 1

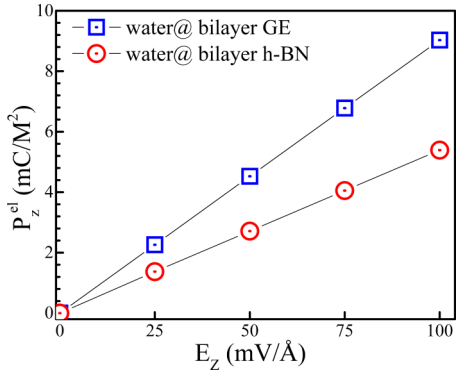

FIG. 2. The z component of the electronic polarization vs applied electric field E_z, of confined water in bilayer GE and bilayer hBN, for interlayer distance $h = 7.2$ Å. The results are obtained after averaging over 100 structural snapshots.

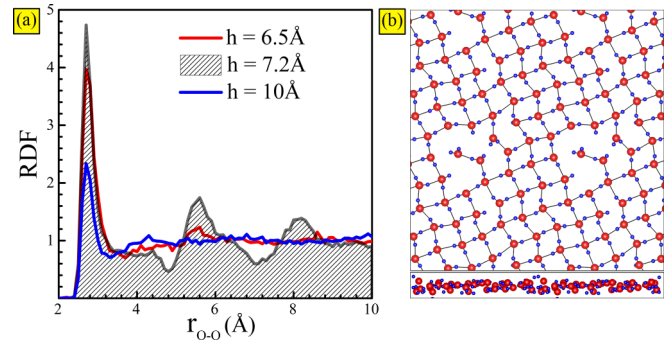

FIG. 4. (a) The radial distribution function of oxygen atoms of confined water for the channel heights $h = 6.5$ Å, 7.2 Å, and 10 Å. Panel (b) shows the top and side views of the lattice structure of confined water for $h = 7.2$ Å.

appears in both $\varepsilon_\perp^{dip}$ and $\varepsilon_\perp^{el}$. One can see that total dielectric constant of confined water is smaller than 2.5 for a wide range of channel heights, i.e., 6.5 Å $\leqslant h \leqslant$ 15 Å. This is in good agreement with the dielectric constant of the angstrom scale channels in the recent experimental data [7]. Notice also that $\varepsilon_\perp^{dip} > 2\varepsilon_\perp^{el}$.

It is further important to note that confined water in channel heights $h \approx$ (7.2–7.5) Å exhibits amorphous crystalline structure (see the shaded area in Fig. 4). To verify this, in Fig. 4(a) we depict the lateral radial distribution function (RDF) of the O-O distance of water molecules confined in channels of height $h = 6.5$ Å, 7.2 Å, and 10 Å. In Fig. 4(b) the lattice structure of confined water in case $h = 7.2$ Å is shown. Such a clear crystalline structure causes the dielectric constant to be minimal and is not observed for other channel heights ($h =$ 6.5 Å or 10 Å). In fact, the electronic and dipolar dielectric constants for $h \approx$ (7.2–7.5) Å are smaller than those found in the other channel heights. We attribute this to the suppression of both electronic charge and molecular dipole fluctuations in the systems with pronouncedly crystalline structure and significant increase in the number of hydrogen bonds, as shown in Fig. 5.

III. DIELECTRIC CONSTANT OF BILAYER GRAPHENE AND BILAYER HBN: THE EFFECT OF INTERLAYER DISTANCE

In this section we turn our attention to finding the dielectric constant of bilayer GE and bilayer hBN, as typical experimental choices for confining membranes in nanofluidic samples.

A. Methodology

For the fully first-principles calculations of dielectric constant of crystalline structure of both GE and hBN, it is more accurate to employ a plane-wave basis projector augmented wave (PAW) method in the framework of density-functional theory (DFT). The generalized gradient approximation (GGA) in the Perdew-Burke-Ernzerhof (PBE) form [24] was used for the exchange-correlation potential as implemented in the Vienna *ab initio* simulation package (VASP) [25]. In order to capture the layer-layer interaction, the vdW correction to the GGA functional was included, by using the DFT-D2 method of Grimme [26].

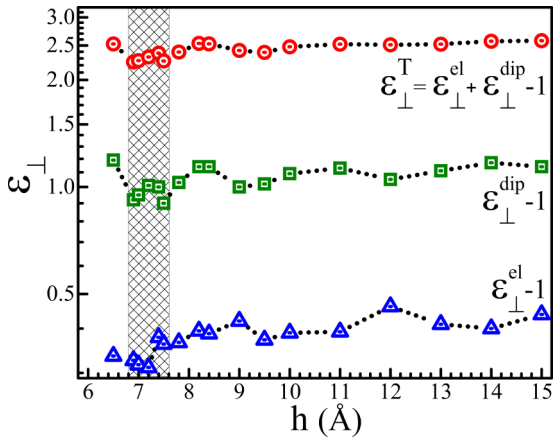

FIG. 3. Electronic, dipolar, and total dielectric constant of confined water as a function of the channel height. Shaded area highlights the minimal values of both $\varepsilon_\perp^{el}$ and $\varepsilon_\perp^{dip}$.

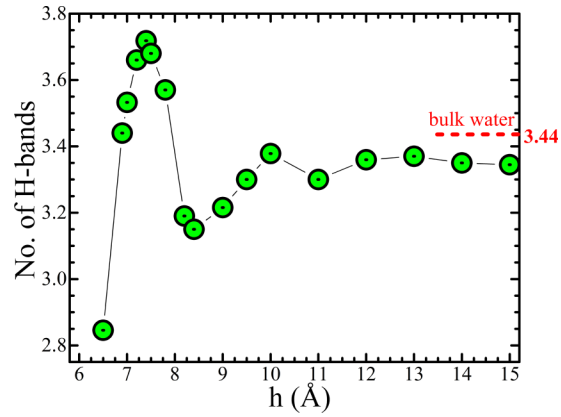

FIG. 5. The variation of the number of H bonds in confined water as a function of the channel height in the MD simulations. The red dashed line indicates the number of hydrogen bonds in bulk water.

For the ground-state stacking configurations of the studied bilayers (GE and hBN), the structural optimizations and the dielectric properties were calculated using the kinetic energy cutoff for plane-wave expansion to be 500 eV. The energy was minimized until its variation in the following steps became 10^{-8} eV. A $50 \times 50 \times 1$ Γ-centered k-point sampling was used for both structural optimizations and dielectric properties. To avoid interaction between the neighboring layers, a vacuum space of 20 Å was implemented. The atoms were fully relaxed until the stress along each direction became smaller than 1 kbar and the forces acting on each atom became less than 10^{-8} eV/Å.

Used two-dimensional membranes exhibit periodicity in two directions (x and y directions in our calculations) and the layer is confined in the z direction. Nonphysical interactions are avoided by introducing a vacuum between the repeating layers in the z direction. The output of the VASP code for the dielectric constant, $\varepsilon^{\rm SC}$, then contains both the dielectric response of the layer and the effect of the inserted vacuum. The 3×3 dielectric constant has three nonzero elements, two in-plane ($\varepsilon^{\rm SC}_{xx} = \varepsilon^{\rm SC}_{yy}$) and one out-of-plane ($\varepsilon^{\rm SC}_{zz}$) component. VASP calculates the electronic dielectric constant using the following equation

$$\varepsilon^{\rm SC}_{ij} = \left(\delta_{ij} + \chi^{\rm el}_{ij}\right), \tag{4}$$

where indices $i, j = x, y, z$, $\varepsilon^{\rm SC}_{ij}$ represents the dielectric constant for the ij direction, while $\chi^{\rm el}_{ij}$ is the susceptibility tensor for the same direction. Due to the isotropic nature of the bilayers, the dielectric constant elements are zero for $i \neq j$. Notably, the dielectric constant given in Eq. (4) includes the electronic and ionic contributions which are given by the susceptibility tensor:

$$\chi^{\rm el}_{ij} = \chi^{\rm el}_{ij} + (1/V) Z_{mi} F^{-1}_{mn} Z_{nj}, \tag{5}$$

where m, n count the atoms in the lattice, $\chi^{\rm el}_{ij}$ is the pure electronic susceptibility tensor, V is the volume of the cell, F^{-1}_{mn} is the force constant matrix, and Z is the Born effective charge tensor.

Note that the dielectric constants extracted from VASP represent the combined dielectric constant of the sample and the surrounding vacuum. In order to distill the dielectric constant of the sample alone, we eliminate the contribution of the vacuum using a capacitance model [6]. In fact, in the out-of-plane direction, the capacitance of the supercell extracted directly from VASP code ($\varepsilon^{\rm SC}_{\perp}$) is the series of the vacuum capacitance and the sample capacitance. This enables us to find the out-of-plane electronic dielectric constant (we used notation $zz = \perp$) of the sample alone using [6]

$$\varepsilon^{\rm el}_{\perp} = \left[1 + \frac{c}{t}\left(\frac{1}{\varepsilon^{\rm SC}_{\perp}} - 1\right)\right]^{-1}, \tag{6}$$

where c is the thickness of the supercell (including the sample and the surrounding vacuum) and t is the real thickness of the system [see Fig. 1(d)], i.e., $t = h + \sigma$. Therefore all the results reported in this paper using VASP code have been re-scaled using Eq. (6).

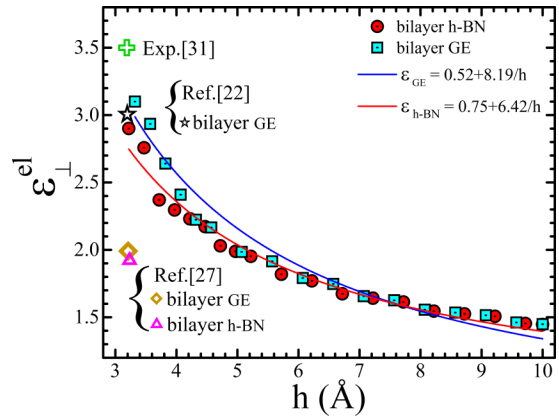

FIG. 6. The obtained electronic dielectric constant ($\varepsilon^{\rm el}_{\perp}$) of bilayer GE and bilayer hBN vs the channel height, in comparison to several available values from literature.

B. Results

Finally we discuss the calculated electronic dielectric constant of bilayer GE and bilayer hBN as confining membranes. We performed several *ab initio* simulations for determining the dielectric constant of bilayer GE (with AB stacking) and hBN (with AA′ stacking) as a function of interlayer distance. Here the evaluations of dielectric constant are done at zero temperature and for rigid bilayers, hence the dipolar term for the dielectric constant is zero.

For the ground-state bilayers, there are few available reports on the dielectric constant using different thickness for monolayer and bilayer GE and bilayer hBN [6]. Our results of $\varepsilon^{\rm el}_{\perp}$ for bilayer GE and bilayer hBN (3.0) are in good agreement with those of Ref. [27], i.e., $\varepsilon^{\rm el}_{\perp} \simeq 2.9$ and the experimental results for the total dielectric constant [7,28], i.e., $\varepsilon^{T}_{\perp} \cong 3.5$. In comparison to our results, Ref. [29] underestimates $\varepsilon^{\rm el}_{\perp}$ for bilayer GE and bilayer hBN. All these results are shown in Fig. 6(a).

The variation of $\varepsilon^{\rm el}_{\perp}$ with h representing a decay function. This is due to the fact that, as seen from Eq. (2), the dielectric constant is a function of thickness via $V = A \times t$. Therefore one expects to see a decreasing function of $\varepsilon^{\rm el}_{\perp}$ with increasing interlayer distance h, as validated in our results shown in Fig. 6(a). Two best fits according to Eq. (2) and corresponding functions are shown by solid lines in Fig. 6(a), i.e., $\varepsilon^{\rm el}_{\perp}({\rm GE}) = 0.52 + 8.19/h$ and $\varepsilon^{\rm el}_{\perp}({\rm hBN}) = 0.75 + 6.42/h$. We speculate that the main origin of the decreasing dependence of $\varepsilon^{\rm el}_{\perp}$ on thickness is the induced charge polarization in bilayers driven by external electric field.

For completeness of the analysis, we performed two additional DFT calculations to determine the electronic dielectric constant of monolayer GE and hBN, and obtained values 2.94 and 2.99, respectively. These values are very close to those found for relaxed bilayer GE and bilayer hBN [the starting values at far left of Fig. 6(a)]. This can be understood by using a simple model for a bilayer with dielectric constant $\varepsilon_{\rm BL}$ composed of two successive capacitors, each made of a monolayer with dielectric constant $\varepsilon_{\rm ML}$. Taking the thickness of the bilayer as $t_{\rm BL}$ and that of monolayers as $t_{\rm ML}$, and the fact that $C_{\rm BL} = C_{\rm ML}/2$ for a series of two capacitors, one writes $t_{\rm BL}/\varepsilon_{\rm BL} = 2 \times t_{\rm ML}/\varepsilon_{\rm ML}$. Using $t_{\rm BL} = 2 \times t_{\rm ML}$—when

the bilayer is at its minimum energy configuration—we find $\varepsilon_{\mathrm{BL}} = \varepsilon_{\mathrm{ML}}$. This is indeed verified by our *ab initio* results and once more validates our methodology.

IV. OPTICAL PROPERTIES

In this section, we connect the dielectric function of the studied systems to their corresponding optical properties, in particular the absorption spectra, the electron energy loss function, and the real part of the dielectric function. When discussing properties of the confining membranes we consider monolayer, bilayer, and double-layer GE. Here the term 'double layer' stands for two GE layers which are separated by an arbitrary channel width $h > 3.5$ Å. The term 'bilayer' refers to the minimum-energy configuration of two stacked graphene layers, i.e., AB stacking for bilayer GE (with $h = 3.4$ Å).

A. Method

The dielectric function $\varepsilon(\omega)$ is obtained by assuming $\lambda \gg L_{\mathrm{uc}}$, where λ and L_{uc} are the wavelength of the incident light and the unit cell length, respectively. The imaginary part $[\varepsilon_i(\omega)]$ of $\varepsilon(\omega)$ is extracted using the Lorentzian approximation of Dirac delta function [30], and the real part $[\varepsilon_r(\omega)]$ can be obtained using the Kramers-Kronig relations [31]. It is useful to mention that $\varepsilon_r(\omega)$ and $\varepsilon_i(\omega)$ are related to the energy storage and dielectric losses within the medium, respectively. Consequently, the extinction ratio $\kappa(\omega)$ is given as:

$$\kappa(\omega) = \sqrt{\frac{\sqrt{\varepsilon_r^2(\omega) + \varepsilon_i^2(\omega)} - \varepsilon_r(\omega)}{2}}, \tag{7}$$

from which the absorption spectrum $\alpha(\omega)$ can be calculated as:

$$\alpha(\omega) = \frac{2\omega\kappa(\omega)}{c}, \tag{8}$$

where λ and c are wavelength and speed of light in vacuum, respectively. Three different absorption spectra can be obtained with respect to the polarization direction of the external electric field. The broadening energy and the value of the scissor operator are taken as 50 meV and 1 eV, respectively. The electron energy loss (EEL) function (the collective excitation of plasma) is calculated as follows:

$$L(\omega) = \mathrm{Im}\left(-\frac{1}{\varepsilon(\omega)}\right) = \frac{\varepsilon_i(\omega)}{\varepsilon_r^2(\omega) + \varepsilon_i^2(\omega)}, \tag{9}$$

where $L(\omega)$ gives the electron inelastic interaction with a sample.

B. Results

1. Energy loss function of confined water

We first calculated the electron energy loss function for confined water between GE sheets. As a general feature, we find that confined water exhibits a large redshift and a strong decrease of intensity of the characteristic peak compared to bulk water [see Fig. 7(a)]. For example, the characteristic peak for confined water in 7.2 Å channel appears at energy about 16 eV [with $\lambda \cong 77$ nm and $\nu = 3.87 \times 10^{15}$ Hz in the extreme ultraviolet (EUV) range]. The peak broadening

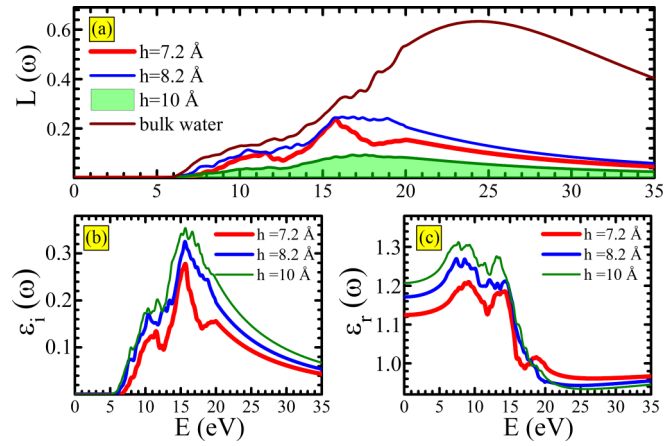

FIG. 7. (a) Total electron loss function, (b) imaginary part, and (c) real part of the electric dielectric function of confined water in angstrom-scale slits. Here the heights of the channel are 7.2 Å, 8.2 Å, 10 Å. For comparison purposes we show bulk results.

and a slight blueshift is observed with increasing channel height, which is due to the phase transition from amorphous ice to liquid water. The characteristic peak for bulk water is located at energy about 25 eV (with $\lambda \cong 49.5$ nm and $\nu = 6.05 \times 10^{15}$ Hz in the same EUV range). Our results for bulk water are in agreement with those reported by Emfietzoglou *et al.* using an optical-data model [32] and with those obtained in inelastic scattering measurements [33]. One should note that the significant peak, in this work, appears beyond the range (0–20) eV at energy about 25 eV compared to the results in Refs. [34,35].

The reason for the larger $L(\omega)$ in bulk water as compared to the confined water is the larger degree of freedom of water molecules in bulk water resulting in larger fluctuations in the electronic polarization ($\Delta\mu_z^{\mathrm{el}}$). The latter increases the dipolar term in Eq. (3). In addition, we depicted real and imaginary parts of electric dielectric function for confined water between GE sheets, i.e., $\varepsilon_r(\omega)$ and $\varepsilon_i(\omega)$ as shown in Figs. 7(b) and 7(c). It is seen that $\varepsilon_r(\omega)$ and $\varepsilon_i(\omega)$ for channel height 10 Å is larger than those for 7.2 Å, 8.2 Å. Subsequently $L(\omega)$ is also smaller for the channel with height 10 Å.

Furthermore, the calculated energy gaps for confined water were 3.86 eV, 4.71 eV, and 4.56 eV for channel heights $h = 7.2$ Å, 8.2 Å, 10 Å, respectively. Such nonmonotonic behavior of the band gap can be related to the (in)commensurability between the channel height and the size of water molecules [34].

Also, the absorption coefficient was calculated. The optical gap (Δ_o) and the electronic gap (Δ_e) are almost equal, which is due to neglected excitonic effects. As a result, the band edge absorption spectra show nonmonotonic (oscillating) behavior for both Δ_e and Δ_o. Notice that no absorption peak was found for either confined or bulk water, which is due to the transparency of water at the absorption edge. We refrain from repeating those results here.

2. Energy loss function of graphene membranes

As a highly spatially resolved spectroscopy (SRS) to detect changes in the electronic structure, the electron loss function

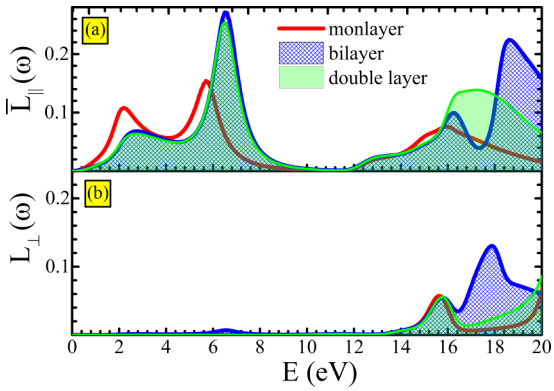

FIG. 8. Electron energy loss function for monolayer, bilayer, and double-layer GE for (a) in-plane polarization and (b) perpendicular polarization.

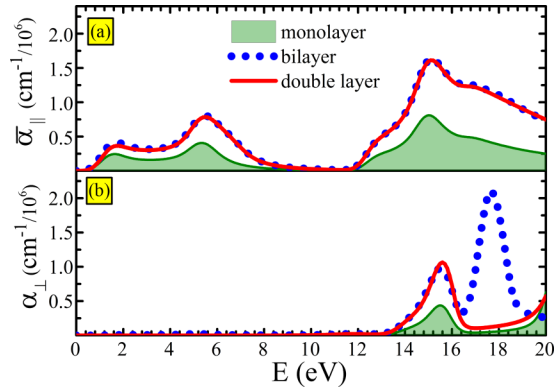

FIG. 9. The absorption spectra for monolayer, bilayer, and double-layer GE along (a) in-plane polarization and (b) perpendicular polarization.

is a very suitable approach to investigate the surface plasmons. There are two types of surface plasmons: (i) low energy 2D plasmons and (ii) high energy π and $\pi + \sigma$ plasmons [36,37]. The electronic structure could be found by recording the energy loss of transmitted or reflected electrons. Also, these surface plasmons can be described using the classical plasmons theory [38]. In fact, the energy of plasmons can be calculated from the peak positions of any loss function. Multiple peaks are found in the electron loss function because of the collective excitations at various photon energies. In Fig. 8, EEL functions [$\bar{L}_{\parallel}(\omega)$ and $L_z(\omega)$] are shown for monolayer, bilayer, and double-layer GE along three different photon polarization directions (x, y, and z). The revealed peaks in $\bar{L}_{\parallel}(\omega)$ and $L_z(\omega)$ display plasma frequencies (ω_p).

Duo to the symmetry, the EEL function for the x and y directions are the same. Figure 8(a) shows the in-plane EEL function ($\bar{L}_{\parallel}(\omega) = \frac{L_x(\omega)+L_y(\omega)}{2}$). Three peaks of $\bar{L}_{\parallel}(\omega)$ are found at 2 eV, 5.6 eV, and 16 eV in monolayer GE, which is in good agreement with previous reports [39–41]. The first peak (at ~2 eV) originates from the π plasmon. The other peaks are due to the $\pi + \sigma$ plasmons. Going from monolayer to bilayer and double-layer GE, one notices a blueshift in both relevant energy ranges, with double-layer data somewhat redshifted with respect to bilayer data. Further, the peak at 2 eV of the monolayer is washed out in cases of bilayer and double layer. We note that the optical properties remain similar for channel heights in the range 5 Å $\leqslant h \leqslant$ 10 Å, so only $h = 5$ Å was considered for the double-layer case in our calculations.

In Fig. 8(b) we plot the EEL function for the perpendicular polarization (z-polarized photon). $L_z(\omega)$ is forbidden in IR and visible range when the electric field is perpendicular to the GE sheets. The results remain relatively unchanged in the UV range, compared to the other directions of photon polarization. It is important to note that the peaks in $L_z(\omega)$ could stem from the resonant transitions of π, π^*, σ, and σ^* electrons among bands in all directions. In addition, the high energy π and $\pi + \sigma$ plasmons can be found in bilayer and multilayer GE [42].

3. Optical absorption of graphene membranes

Optical absorption of GE is divided into intraband (from IR to vacuum-UV) and interband transitions (in the extreme-UV range). Allowed optical transitions between subbands obey relation $|N| = |M \pm 1|$, where N and M are Landau level indices [43]. In Fig. 9, strong optical isotropic in the monolayer, bilayer, and double-layer GE is shown for the polarization vector on sheet.

Duo to the symmetry, the absorption for the x and y directions is the same. Figure 9(a) show in-plane optical absorption ($\bar{\alpha}_{\parallel} = \frac{\alpha_x+\alpha_y}{2}$). Absorption takes place from IR to UV range. We found a symmetry-allowed peak at 5.2 eV [44], although earlier empirical results indicated an asymmetric absorption peak at 4.6 eV [45–48] in deep-UV range (related to intraband transitions). Additionally, we did not find the second exciton peak at 6.4 eV reported in Ref. [42]. These differences originate from excitonic effects. In addition, quasiflat bands of π and π^* cause (i) the electron and hole effective masses to become larger, (ii) van Hove singularities to appear closer to the Fermi level, and (iii) the absorption peak to emerge in the deep-UV range [39], along M-K symmetry direction. Furthermore, asymmetric absorption peaks have been observed related to interband transitions in extreme-UV range. For monolayer GE, the maximum intensity absorption peak is found at ~15 eV which originates from the electronic transition between p_x hybridized orbital and π^* antibonding orbital along the M-K direction and around K point, respectively [39]. Also, we found a slight blueshift and an intensity increase in the bilayer and double-layer GE compared to the monolayer GE. Additionally, we did not find the peak at 12 eV in monolayer GE, due to parallel bands p_y to π^* along K-Γ direction, reported in Ref. [46].

Figure 9(b) shows the absorption for perpendicular polarization (z-polarized photon), which is negligible (from IR to vacuum-UV) because of the extremely small thickness of the layers. The first absorption peak is observed at 15.6 eV for all considered GE membranes. A sharp absorption peak around 17.6 eV was found in bilayer GE that can be related to the electron charge redistribution caused by an external perturbation (e.g., incident light). In fact, AB-stacked configuration causes asymmetry between valence and conduction bands. Therefore, charge transfer occurs between upper and bottom layers, after spatial redistribution of the electron density [49,50]. Consequently, both the

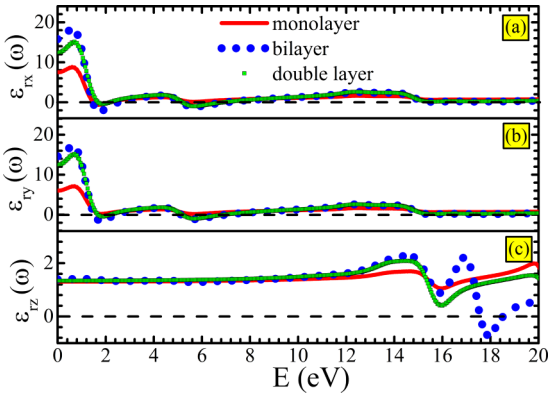

FIG. 10. Real part of the dielectric function for monolayer, bilayer, and double-layer GE, for photon polarization along the (a) x, (b) y, and (c) z direction.

intensity of interlayer transitions and the absorption peak are enhanced in the extreme-UV range.

4. The real part of the dielectric function of graphene membranes

The static dielectric function [$\varepsilon(0)$] refers to response of the system to the external electric field at near-zero frequencies. Figure 10(a) shows the real part of the dielectric function for the x-polarized photon. $\varepsilon(0)$ is about 7.5 eV, 15.6 eV, and 12.4 eV for monolayer, bilayer, and double-layer GE, respectively. Moreover, the typical oscillatory behavior of the dielectric function is dampened in all cases, for energies above 6 eV. Furthermore, the plasmon frequency (ω_p) can be found where ε_r changes sign from negative to positive [51]. There is one plasmon frequency in monolayer GE at 2.6 eV and two different plasmon frequencies in the bilayer and double-layer GE at 2.6 eV and 6.7 eV.

Figure 10(b) shows the real part of the dielectric constant for the y-polarized photon. The static $\varepsilon(0)$ is about 6 eV, 14.6 eV, and 12.4 eV for monolayer, bilayer, and double-layer GE, respectively. For y polarization, two plasmon frequencies are found for both bilayer and double-layer GE at 2.6 eV and 6.7 eV, but there is still no plasmon frequency in the monolayer case.

For the z-polarized photon [Fig. 10(c)], static $\varepsilon(0)$ is about 1.3 eV, 1.38 eV, and 1.34 eV for monolayer, bilayer, and double-layer GE, respectively. These values are close to the vacuum dielectric function, due to the extremely small thickness of the material along the z direction. The oscillatory behavior of the real part of the dielectric constant shifts into the extreme-UV range and starts from 13 eV. The plasmon frequency is found only for bilayer GE, at 18.5 eV. As mentioned above, the perpendicular electric field causes the asymmetry of the charge redistribution around atoms of upper and bottom layers in bilayer GE [49,50], which causes optical differences compared to monolayer GE.

V. CONCLUDING REMARKS

Fumagalli *et al.* were recently able to experimentally extract the out-of-plane dielectric constant $\varepsilon_\perp^T$ of confined water in bilayer hBN [7]. However, it remained unanswered what the electronic and dipolar contributions are to dielectric constant of confined water. For bulk water ($\varepsilon_B = 80$), because of the large dielectric constant, one knows that the electronic contribution is negligible [35].

On the other hand, in a metallic 2D crystal, because of perfect crystalline structure, one expects to have nearly 100% of $\varepsilon_\perp^T$ to be the electronic contribution [6]. However, when water is confined between two 2D membranes, in angstrom-scale slits, the ultralow $\varepsilon_\perp^T$ ($\approx$2.1) makes it highly nontrivial to determine the ratio between the electronic and dipolar terms. After recovering the experimental result for $\varepsilon_\perp^T$ in our simulations of water confined in bilayer GE and bilayer hBN, in this paper we revealed that over 40% of the total dielectric constant of confined water in angstrom-scale slits is the electronic contribution. In other words, dipolar and electronic parts of dielectric constant become very comparable in strongly confined water. The small dielectric constant can be attributed to the reduced number of hydrogen bonds of confined water in angstrom-scale slits, i.e., the preferential tetrahedral bonding geometry in bulk water and ice are no longer favored. Moreover our results confirm that the lattice structure of the confined water in recent experiment does not correspond to any of the previously studied 2D ices [52] and has likely random structure. Therefore, one should not expect to recover experimental data when studying monolayer crystalline ice.

For completeness, we also determined the electronic dielectric constant of bilayer GE and hBN as typical confining membranes, as a function of the interlayer spacing, and showed that it decreases with increasing the interlayer distance. The obtained value for standard (empty) bilayer is also in excellent agreement with available experimental data—the measured dielectric constant of bilayers in recent experiment is about $\varepsilon_\perp^T \approx 3.5$ which is very close to our value $\varepsilon_\perp^{\rm el} = 3.0$. The difference is likely due to the finite temperature dipolar term that can be added to our analysis. In fact at finite temperatures, bilayers are not rigid and one expects to see angstrom-scale ripples. The latter will yield nonzero dipolar term for the dielectric constant of bilayers.

In the last part of this paper we analyzed the optical properties of both confined water and bilayer/monolayer and double-layer GE as confining membranes. In particular, we showed that electron energy loss function of confined water is very different compared to bulk water. Though the characteristic peak for bulk water locates at energy about 25 eV, it shifts to about 16 eV for confined water in 7.2 Å slits. With increasing channel height (i.e., 7.2 Å $< h \leqslant$ 15 Å.), we observe a peak broadening and a slight blueshift due to the phase transition from amorphous ice to liquid water. Concerning the membranes, we detail the differences between monolayer, bilayer, and double-layer graphene when exposed to incident light in different directions.

We conclude that the use of our methodology is fully corroborated by comparison to experimental data and that it reliably discriminates the electronic and dipolar contributions to dielectric constant of confined water. Taken together with reported optical properties of all system constituents,

our results are very important for further understanding of optoelectronic properties of water and its interactions with surfaces and fields but also for understanding such properties of other fluids and solids under extreme confinement.

ACKNOWLEDGMENTS

This work was supported by the Research Foundation - Flanders (FWO). M.Y. gratefully acknowledges his FWO postdoctoral mandate.

[1] Y. Zhou, J. H. Morais-Cabral, A. Kaufman, and R. MacKinnon, Nature (London) **414**, 43 (2001).

[2] B. L. de Groot and H. Grubmüller, Science **294**, 5550 (2001).

[3] R. F. Giese and C. J. Van Oss, *Colloid and Surface Properties of Clays and Related Minerals* (CRC Press, 2002).

[4] Z. Siwy, I. D. Kosińska, A. Fuliński, and C. R. Martin, Phys. Rev. Lett. **94**, 048102 (2005).

[5] H. Daiguji, P. Yang, and A. Majumdar, Nano Lett. **4**, 137 (2004).

[6] A. Laturia, M. L. Van de Put, and W. G. Vandenberghe, npj 2D Mater. Appl. **2**, 1 (2018).

[7] L. Fumagalli, A. Esfandiar, R. Fabregas, S. Hu, P. Ares, A. Janardanan, Q. Yang, B. Radha, T. Taniguchi, K. Watanabe, G. Gomila, K. S. Novoselov, and G. Gomila, Science **360**, 1339 (2018).

[8] M. Sobrino Fernández, F. M. Peeters, and M. Neek-Amal, Phys. Rev. B **94**, 045436 (2016).

[9] H. Itoh and H. Sakuma, J. Chem. Phys. **142**, 184703 (2015).

[10] C. Zhang, F. Gygi, and G. Galli, J. Phys. Chem. Lett. **4**, 2477 (2013).

[11] V. Ballenegger and J. P. Hansen, J. Chem. Phys. **122**, 114711 (2005).

[12] A. Schlaich, E. W. Knapp, and R. R. Netz, Phys. Rev. Lett. **117**, 048001 (2016).

[13] S. Ghasemi, M. Alihosseini, F. Peymanirad, H. Jalali, S. A. Ketabi, F. Khoeini, and M. Neek-Amal, Phys. Rev. B **101**, 184202 (2020).

[14] S. Plimpton, J. Comput. Phys. **117**, 1 (1995).

[15] S. Nose, J. Chem. Phys. **81**, 511 (1984).

[16] H. J. C. Berendsen, J. R. Grigera, and T. P. Straatsma, J. Chem. Phys. **91**, 6269 (1987).

[17] J. P. Ryckaert, G. Ciccotti, and H. J. Berendsen, J. Comput. Phys. **23**, 327 (1977).

[18] P. M. Morse, *Thermal Physics* (W. A. Benjamin, New York, 1969).

[19] J. M. Soler, E. Artacho, J. D. Gale, A. Garca, J. Junquera, P. Ordejn, and D. Snchez-Portal, J. Phys.: Condens. Matter **14**, 2745 (2002).

[20] R. Elmér, M. Berg, L. Carlén, B. Jakobsson, B. Norén, A. Oskarsson, G. Ericsson, J. Julien, T.-F. Thorsteinsen, M. Guttormsen, G. Løvhøiden, V. Bellini, E. Grosse, C. Müntz, P. Senger, and L. Westerberg, Phys. Rev. Lett. **78**, 1396(E) (1997).

[21] M. Dion, H. Rydberg, E. Schröder, D. C. Langreth, and B. I. Lundqvist, Phys. Rev. Lett. **92**, 246401 (2004); Erratum: **95**, 109902 (2005).

[22] P. Umari and A. Pasquarello, Phys. Rev. Lett. **89**, 157602 (2002).

[23] W. L. Jorgensen, J. Chandrasekhar, J. D. Madura, R. W. Impey, and M. L. Klein, J. Chem. Phys. **79**, 926 (1983).

[24] J. P. Perdew, K. Burke, and M. Ernzerhof, Phys. Rev. Lett. **77**, 3865 (1996).

[25] G. Kresse and J. Hafner, Phys. Rev. B **47**, 558 (1993).

[26] S. J. Grimme, J. Comput. Chem. **27**, 1787 (2006).

[27] E. J. G. Santos and K. Efthimios, Nano Lett. **13**, 898 (2013).

[28] K. K. Kim, A. Hsu, X. Jia, S. M. Kim, Y. Shi, M. Dresselhaus, T. Palacios, and J. Kong, ACS Nano **6**, 8583 (2012).

[29] P. Kumar, Y. S. Chauhan, A. Agarwal, and S. Bhowmick, J. Phys. Chem. C **120**, 17620 (2016).

[30] G. D. Sanders and Y. C. Chang, Phys. Rev. B **45**, 9202 (1992).

[31] E. Rosencher and B. Vinter, *Optoelectronics* (Cambridge University Press, Cambridge, 2002).

[32] D. Emfietzoglou, I. Kyriakou, I. Abril, R. Garcia-Molina, and H. Nikjoo, Int. J. Radiat. Biol. **88**, 22 (2012).

[33] J. M. Heller Jr, R. N. Hamm, R. D. Birkhoff, and L. R. Painter, J. Chem. Phys. **60**, 3483 (1974).

[34] M. Neek-Amal, F. M. Peeters, I. V. Grigorieva, and A. K. Geim, ACS Nano **10**, 3685 (2016).

[35] D. C. Elton, Ph.D. thesis, Stony Brook University, Stony Brook, NY, 2016.

[36] A. Muñoz, J. C. Oller, F. Blanco, J. D. Gorfinkiel, P. Limão-Vieira, and G. García, Phys. Rev. A **76**, 052707 (2007).

[37] X. Luo, T. Qiu, W. Lu, and Z. Ni, Mater. Sci. Eng. R: Rep. **74**, 351 (2013).

[38] A. Y. A. T. O. Nagashima, K. Nuka, H. Itoh, T. Ichinokawa, C. Oshima, S. Otani, and Y. Ishizawa, Solid State Commun. **83**, 581 (1992).

[39] R. John and B. Merlin, J. Phys. Chem. Solids **110**, 307 (2017).

[40] T. Eberlein, U. Bangert, R. R. Nair, R. Jones, M. Gass, A. L. Bleloch, K. S. Novoselov, A. Geim, and P. R. Briddon, Phys. Rev. B **77**, 233406 (2008).

[41] A. G. Marinopoulos, L. Reining, A. Rubio, and V. Olevano, Phys. Rev. B **69**, 245419 (2004).

[42] V. B. Jovanović, I. Radović, D. Borka, and Z. L. Mišković, Phys. Rev. B **84**, 155416 (2011).

[43] A. H. Castro Neto, F. Guinea, N. M. R. Peres, K. S. Novoselov, and A. K. Geim, Rev. Mod. Phys. **81**, 109 (2009).

[44] L. Yang, J. Deslippe, C. H. Park, M. L. Cohen, and S. G. Louie, Phys. Rev. Lett. **103**, 186802 (2009).

[45] D. H. Chae, T. Utikal, S. Weisenburger, H. Giessen, K. V. Klitzing, M. Lippitz, and J. Smet, Nano Lett. **11**, 1379 (2011).

[46] V. G. Kravets, A. N. Grigorenko, R. R. Nair, P. Blake, S. Anissimova, K. S. Novoselov, and A. K. Geim, Phys. Rev. B **81**, 155413 (2010).

[47] W. Li, G. Cheng, Y. Liang, B. Tian, X. Liang, L. Peng, A. H. Walker, D. J. Gundlach, and N. V. Nguyen, Carbon **99**, 348 (2016).

[48] A. N. Grigorenko, M. Polini, and K. S. Novoselov, Nat. Photonics **6**, 749 (2012).

[49] R. N. Wang, G. Y. Dong, S. F. Wang, G. S. Fu, and J. L. Wang, AIP Adv. **6**, 035213 (2016).

[50] T. Ohta, A. Bostwick, T. Seyller, K. Horn, and E. Rotenberg, Science **313**, 951 (2006).

[51] G. Dresselhaus and M. S. Dresselhaus, Magneto-optical effects in solids, in *Optical Properties of Solids*, edited by J. Tauc (Academic Press, New York, 1966).

[52] J. Chen, G. Schusteritsch, C. J. Pickard, C. G. Salzmann, and A. Michaelides, Phys. Rev. Lett. **116**, 025501 (2016).